UNCLASSIFIED

AD NUMBER

ADB264544

NEW LIMITATION CHANGE

TO
Approved for public release, distribution unlimited

FROM
Distribution authorized to U.S. Gov't. agencies only; Proprietary Info.; Jun 1999. Other requests shall be referred to U.S. Army Medical Research and Materiel Command, 504 Scott Street, Fort Detrick, MD 21702-5012.

AUTHORITY

USAMRMC ltr, 23 Aug 2001

AD_____

GRANT NUMBER DAMD17-98-1-8129

TITLE: Nano-Phosphor Grid Screens for Mammography

PRINCIPAL INVESTIGATOR: Rameshwar N. Bhargava, Ph.D.

CONTRACTING ORGANIZATION: Nanocrystals Technology Ltd Partnership
                          Briarcliff Manor, New York 10510

REPORT DATE: June 1999

TYPE OF REPORT: Final

PREPARED FOR: Commanding General
                U.S. Army Medical Research and Materiel Command
                Fort Detrick, Maryland 21702-5012

DISTRIBUTION STATEMENT: Distribution authorized to U.S. Government
agencies only (proprietary information, Jun 99). Other requests
for this document shall be referred to U.S. Army Medical Research
and Materiel Command, 504 Scott Street, Fort Detrick, Maryland
21702-5012.

The views, opinions and/or findings contained in this report are
those of the author(s) and should not be construed as an official
Department of the Army position, policy or decision unless so
designated by other documentation.

20010323 036

NOTICE

THIS TECHNICAL REPORT HAS BEEN REVIEWED AND IS APPROVED FOR PUBLICATION.

02/15/01

REPORT DOCUMENTATION PAGE

Public reporting burden for this collection of information is estimated to average 1 hour per response, including the time for reviewing instructions, searching existing data sources, gathering and maintaining the data needed, and completing and reviewing the collection of information. Send comments regarding this burden estimate or any other aspect of this collection of information, including suggestions for reducing this burden, to Washington Headquarters Services, Directorate for Information Operations and Reports, 1215 Jefferson Davis Highway, Suite 1204, Arlington, VA 22202-4302, and to the Office of Management and Budget, Paperwork Reduction Project (0704-0188), Washington, DC 20503.

1. AGENCY USE ONLY *(Leave blank)*	2. REPORT DATE June 1999	3. REPORT TYPE AND DATES COVERED Final (1 Jun 98 - 31 May 99)

4. TITLE AND SUBTITLE
Nano-Phosphor Grid Screens for Mammography

5. FUNDING NUMBERS
DAMD17-98-1-8129

6. AUTHOR(S)
Rameshwar N. Bhargava, Ph.D.

7. PERFORMING ORGANIZATION NAME(S) AND ADDRESS(ES)
Nanocrystals Technology Ltd Partnership
Briarcliff Manor, New York 10510

8. PERFORMING ORGANIZATION REPORT NUMBER

9. SPONSORING / MONITORING AGENCY NAME(S) AND ADDRESS(ES)
U.S. Army Medical Research and Materiel Command
Fort Detrick, Maryland 21702-5012

10. SPONSORING / MONITORING AGENCY REPORT NUMBER

11. SUPPLEMENTARY NOTES

12a. DISTRIBUTION / AVAILABILITY STATEMENT

Distribution authorized to U.S. Government agencies only
(proprietary information, Jun 99). Other requests for this
document shall be referred to U.S. Army Medical Research
and Materiel Command, 504 Scott Street, Fort Detrick, Maryland 21702-5012.

12b. DISTRIBUTION CODE

13. ABSTRACT *(Maximum 200 words)*

See Next Page

14. SUBJECT TERMS Breast Cancer Nano-phosphor Grid Screen for Mammography	15. NUMBER OF PAGES 30
	16. PRICE CODE

17. SECURITY CLASSIFICATION OF REPORT Unclassified	18. SECURITY CLASSIFICATION OF THIS PAGE Unclassified	19. SECURITY CLASSIFICATION OF ABSTRACT Unclassified	20. LIMITATION OF ABSTRACT Limited

Abstract

The goal of this research is to fabricate X-ray mammography screens with dramatically increased contrast/resolution capabilities. A conventional X-ray phosphor screen has a thickness of about 50 to 200 microns (μm) and consists of phosphor particles with a mean size between 3 to 10 μm. The light generated in the phosphor screen by the incident X-rays scatters over the thickness of the screen material. As the light scatters, it spreads out which results in loss of spatial resolution and contrast.

To overcome the severe light scattering that stems from the phosphor screen thickness, without compromise in X-ray absorption, two approaches have been rigorously investigated. The first approach is to manufacture screens based on a novel type of efficient phosphors: nanocrystalline phosphors. The second approach is to fill microchannel plates with nanocrystalline or micron-sized phosphors. The X-ray-induced light is now transmitted and confined within the microchannel, which operates like an optical-fiber waveguide.

Under X-ray excitation, the nanocrystalline phosphors exhibited luminescence efficiency that is 25% of the standard phosphors. Line-pair-phantom images, obtained from standard-phosphor-filled microchannel-plates of 10-μm diameter size, exhibited a resolution of 40-lp/mm. This resolution is twice that of analog screen/film systems currently used in mammography.

FOREWORD

Opinions, interpretations, conclusions and recommendations are those of the author and are not necessarily endorsed by the U.S. Army.

___✓___ Where copyrighted material is quoted, permission has been obtained to use such material.

___✓___ Where material from documents designated for limited distribution is quoted, permission has been obtained to use the material.

___N/A___ Citations of commercial organizations and trade names in this report do not constitute an official Department of Army endorsement or approval of the products or services of these organizations.

___N/A___ In conducting research using animals, the investigator(s) adhered to the "Guide for the Care and Use of Laboratory Animals," prepared by the Committee on Care and use of Laboratory Animals of the Institute of Laboratory Resources, national Research Council (NIH Publication No. 86-23, Revised 1985).

___N/A___ For the protection of human subjects, the investigator(s) adhered to policies of applicable Federal Law 45 CFR 46.

___N/A___ In conducting research utilizing recombinant DNA technology, the investigator(s) adhered to current guidelines promulgated by the National Institutes of Health.

___N/A___ In the conduct of research utilizing recombinant DNA, the investigator(s) adhered to the NIH Guidelines for Research Involving Recombinant DNA Molecules.

___N/A___ In the conduct of research involving hazardous organisms, the investigator(s) adhered to the CDC-NIH Guide for Biosafety in Microbiological and Biomedical Laboratories.

_____   _____
PI - Signature   Date

TABLE OF CONTENTS

Page

Introduction

The goal of this research is to fabricate X-ray mammography screens with dramatically increased contrast/resolution capabilities. Nanocrystalline phosphor-particle and phosphor-filled microchannel-plate low-scattering screens are the two approaches under investigation. A high contrast/resolution mammography-screen prototype, for use in digital and analog mammography systems, will be the final deliverable.

Importance of X-ray mammography

Presently, the best screening method for breast cancers is X-ray mammography. A number of studies have shown the effectiveness of X-ray mammography screening in reducing breast cancer mortality [1, 2]. In spite of its success, however, X-ray mammography is by no means a perfect test for the detection of breast cancer. Several studies [3-5] have shown that anywhere between 5 to 15% of breast cancers may be missed by mammography. Additionally, the specificity of X-ray mammograms for breast cancer is relatively low. Of the cases recommended for biopsies, on the basis of a X-ray mammogram, only 10 to 50% are cancers [2, 6-8]. Some of these shortcomings are related to the limited contrast and resolution of the screen-film systems currently used.
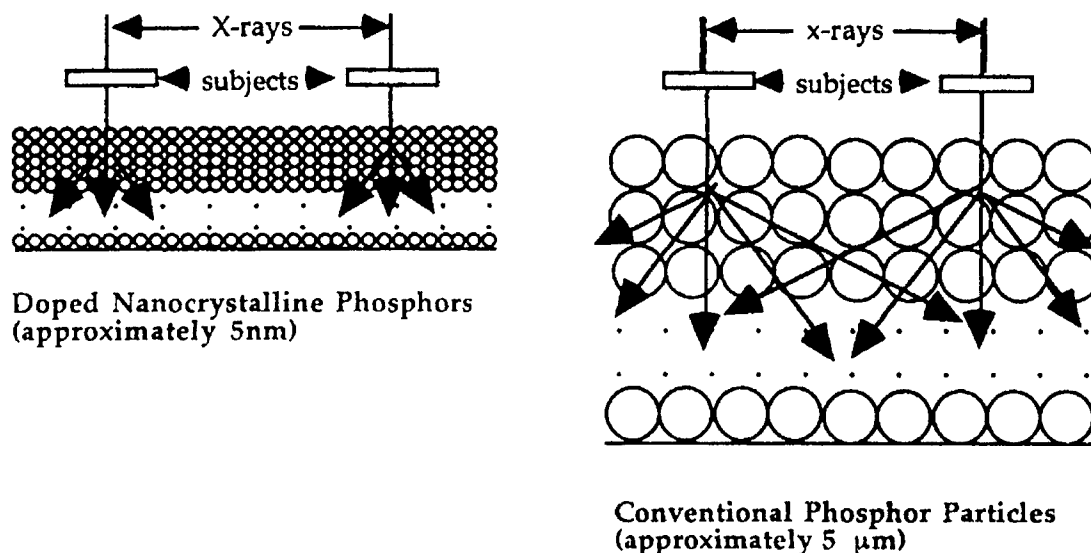
Mammography phosphor-screens

When X-rays pass through a patient, the intensity is modulated by the tissue or bone structure being screened; in other words, the emerging X-ray intensity carries an imprint of the spatial image of the body part being examined. If the recording medium for this image is film, the X-rays must be first converted to visible light in order to expose the film. This is accomplished when X-rays emerging from the anatomy of a patient strike a phosphor-screen, which then emits visible light. The X-ray induced visible-light carries the same imprint as the X-rays. The photographic film underneath the phosphor screen records this imprint as an analog image. In digital recording, the X-ray induced spatial distribution of the visible light is converted to digital signals. Alternatively, the X-ray image signal can be directly converted into electronic charges and its distribution can be mapped by an electronic detector to yield a digital image. Thus, the use of a phosphor screen is imperative for all analog and some (but not all) of digital imaging modalities currently being marketed.

X-ray scattering in mammography screens

A conventional X-ray phosphor screen has a thickness of about 50 to 200 microns (μm) and consists of phosphor particles with a mean size between 3 to 10 μm. The light generated in the phosphor screen by the incident X-rays scatters over the finite thickness of the screen material. As the light scatters, it spreads out which results in loss of spatial resolution and contrast. In general, for high-resolution, high-contrast images, the screens need to be as thin as possible. The use of thin phosphor screens, however, results in low X-ray absorption. Furthermore, use of standard larger-particle (3-10 μm) phosphors in thinner X-ray screens will result in grainy images and poor resolution. Thus, an optimum balance between resolution/contrast and X-ray absorption determines the thickness of the screen.

Doped Nanocrystalline Phosphors
(approximately 5nm)

Conventional Phosphor Particles
(approximately 5 μm)

Figure 1. The spreading of X-ray induced visible light over the thickness of a conventional phosphor screen and a nanophosphor screen. The reduced spreading of light in the nanophosphor screen is due to the decreased scattering by nanosize phosphor particles. This will result in higher resolution images. In a conventional phosphor screen, the visible light experiences greater random scattering typical of larger 3 to 10 μm particles.

The X-ray-induced light is scattered in all directions and diffuses towards the film at the bottom. The profiles of the diffused light originating from two adjacent objects overlap significantly resulting in a blurred image (Fig. 1). Typical phosphor particle-sizes are in the range of 2-10 μm and the thickness of the screen is about 100 μm. In this geometrical arrangement, the light diffuses approximately to 100 μm laterally (50 μm on each side of the object). To distinctly observe the contribution of these two objects, they must be separated by at least 50 μm. This separation of 50 μm (0.05mm) corresponds to a resolution of 1/0.05(mm) = 20 lp/mm. This is the resolution in a typical analog screen.

To overcome the large spreading of light in thick phosphor films, scintillators with high atomic number are used for enhanced X-ray absorption. Although comparatively thin layers of Thallium doped Cesium-Iodide absorb the X-rays and thereby reduce light scattering, they are less efficient in converting the X-ray photons to visible photons. Therefore, the signal to noise ratio and contrast do not improve.

In digital imaging systems, the surface irregularities of the larger particles of the phosphor screen are in a size range between 2 - 5 microns. These irregularities scatter the visible light, which has a wavelength in the range of 0.4 to 0.7 microns. Under such conditions, the random scattering of light cannot be controlled, thus limiting the ability to define a true base-line signal for digitization. The scattering adversely affects the process of digitization and results in a significant reduction of the resolution.

2

**Novel low-scattering X-ray mammography screens**

The goal of our research at NCT is to overcome the severe light scattering that stems from the phosphor screen thickness, without compromise in X-ray absorption. Thus, by lifting the resolution/contrast limitations of present X-ray screens we could greatly improve the capabilities of the mammogram as a detection tool. Two approaches have been rigorously investigated towards that goal. The first approach is to manufacture screens based on a novel type of efficient phosphors: nanocrystalline phosphors. The second approach is to fill microchannel plates with nanocrystalline or micron-sized phosphors. The X-ray-induced light is now transmitted and confined within the microchannel that operates like an optical-fiber waveguide.

Nanocrystalline-Phosphor Screen

The size of nanocrystalline phosphors is in the 2-10 nanometer range, while the wavelength of the X-ray generated visible light is in the 500-700 nanometer range. Since the doped nanocrystalline phosphors are much smaller than the wavelength of light they are expected to behave like a clear liquid which transmits light with negligible scattering. Furthermore, harnessing the quantum-confinement effects that manifest themselves in the nanosize range makes the concept of nanophosphor screens attractive, Appendix A. The concept of a nanophosphor screen has been patented by NCT, Appendix B, patent 1.

Microchannel-Plate Screen

To overcome the severe light scattering that stems from the finite screen thickness, without compromise in X-ray absorption, NCT uses phosphor-filled microchannel plates. Chemical etching of microchannels in a special glass plate creates a grid-structure as shown in Figure 2. Microchannel plates are also made from *Si* wafers. The X-ray-induced light is now transmitted and confined within the microchannel that operates like an optical-fiber waveguide, This is shown in Fig. 3, which depicts the X-ray generated light being internally reflected, confined and propagated within the microchannel of origin.
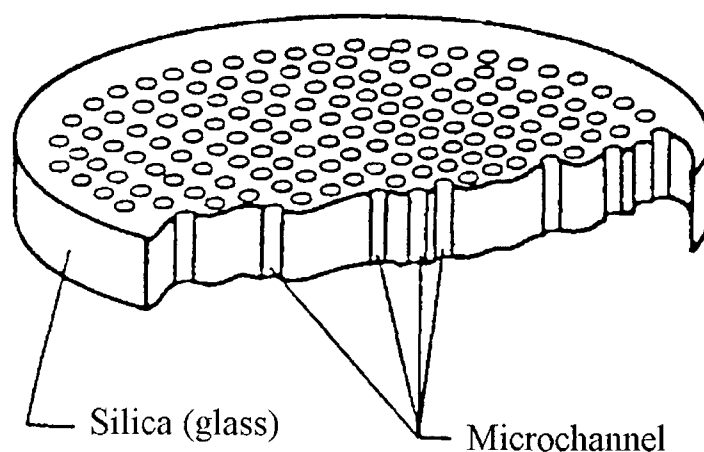
Figure 2. The detailed structure of a microchannel-plate phosphor screen.

A prerequisite for the successful implementation of microchannel-plate screens is the filling of microchannels (5-20 µm diameter and 100-200 µm length) with phosphor particles. Standard-phosphor particle sizes (2-8 µm) as well as nanocrystals may be used to fill the channels. To achieve the needed X-ray absorption, the phosphor particles need to pack densely inside the microchannels.
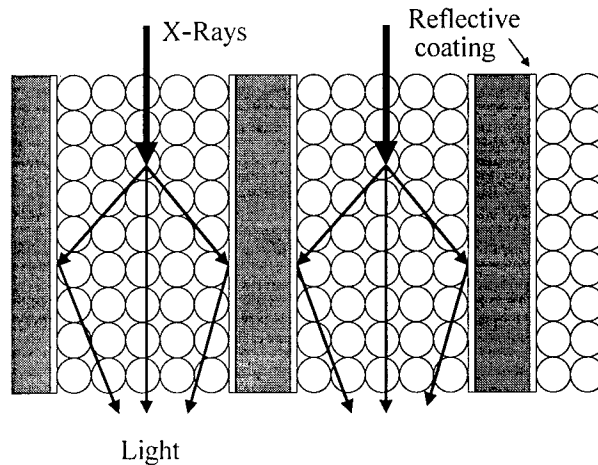
Figure 3. Propagation of X-ray generated visible-light inside the microchannel of origin due to the reflective microchannel wall coating.

To minimize the negative effects of light scattering in microchannel-plate screens, the X-ray generated visible-light must remain within the microchannel of origin. Visible-light "cross-talk" between neighboring microchannels will result in resolution/contrast reduction. To trap the light within the microchannel of origin, microchannel-wall reflective coating techniques are being developed.
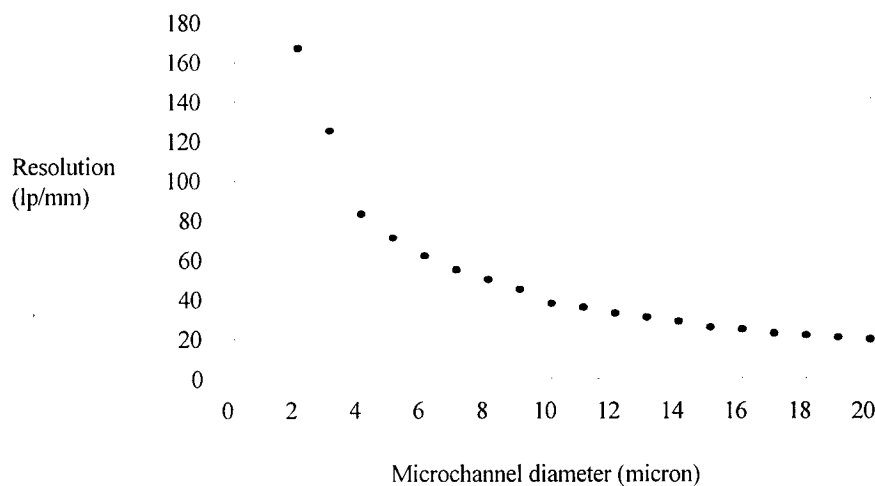
Figure 4. Microchannel-plate resolution as a function of microchannel diameter size.

Microchannels of 10-μm diameter, spaced 2-μm apart, are capable of resolving 42 lp/mm. Reducing the microchannel diameter size to 5-μm results in a resolution capability of 83 lp/mm. The resolution capability of a microchannel plate as a function of the channel diameter is plotted in Fig. 4. The resolution increases rapidly as the size of the microchannel-diameter decreases below 10 microns.

The development of efficient X-ray nanocrystalline phosphors is of critical importance for the implementation of nanocrystalline screens. Also, in the case of microchannels plates, as the microchannel-size is reduced, small-sized phosphor particles are needed (below 3-μm) in order to achieve dense packing. It is for this reason that the first part of this research focused on the preparation and characterization of nanocrystalline phosphors. Additionally, due to the potential for dramatic increase in resolution/contrast in microchannel-plate screens, microchannel phosphor-filling and preliminary resolution measurements were performed.

1st YEAR TASKS

Task 1: Preparation of nanocrystalline phosphors, in the 3-10 nm size range, by sol-gel and micro-emulsion chemical syntheses.

- Preparation of doped nanocrystalline phosphors of green-emitting Y_2O_3:Tb
- Preparation of doped nanocrystalline phosphors of red-emitting PbO:Eu
- Modify the chemical synthesis procedures in accordance with the latest measurement and deposition data.

Sol-gel preparation

Sol-gel processing techniques were used to synthesize Y_2O_3:Tb nanocrystals. First, metallic sodium was reacted with iso-Propanol quantitatively resulting in sodium iso-Propoxide. The latter was reacted with yttrium and terbium chlorides to obtain yttrium and terbium isopropoxides. Yttrium and terbium iso-propoxides were combined in azeotropic distillation of butanol to exchange the iso-propoxide to butoxide groups. A five-fold excess of n-Butanol was used. The resulting yttrium/terbium n-butoxide was used as a stock solution and was combined with yttrium butoxide which was prepared separately to vary the Tb or other dopant concentration in the nanocrystals.

To improve the UV and X-ray luminescence of sol-gel nanophosphors, several synthesis modifications were performed. Two major ones are briefly described below:

One synthesis was based on separate terbium and yttrium precursors. In this process, the concentration of terbium chloride was varied by a fixed amount of yttrium butoxide before the hydrolysis step. This addition replaced the step of synthesizing a mixed yttrium-terbium butoxide used in the acid catalyzed sol-gel method.

Aqueous processing, a totally different preparation method of terbium doped yttrium, with smaller particle size, was explored. In this approach two main parameters were controlled: pH and ionicity. Yttrium and terbium chlorides were used as precursors. The

pH was controlled using HNO_3 and ionicity was varied from 0.5 to 2 M using $NaNO_3$. Sodium hydroxide was used to precipitate the final product.

Sol-gel synthesis of Y_2O_3:Tb nanocrystals is relatively time-consuming and gives low UV and X-ray luminescence. An alternative approach to DNC phosphor synthesis was developed to overcome the acid-catalyzed sol-gel synthesis drawbacks, mainly the inevitable incorporation of organics during the synthesis process. Nanocrystalline Y_2O_3:Tb phosphors were prepared by *microemulsion* techniques. The advantages of this preparation approach are the minimal incorporation of organics, the simple and relatively few preparation steps required, and the guaranteed incorporation of the dopant *Tb* atoms inside the nanocrystals. Excellent control of nanocrystalline particle-size, uniformity of particle-size, and reproducibility are additional advantages that make microemulsion very suitable for the preparation of Y_2O_3:Tb, PbO:Tb and Gd_2O_3:Tb nanocrystals.

Micro-emulsion preparation

Micelles, microemulsion and vesicles can be used as microreactors to carry out chemical reactions in confined geometry. Water-in-Oil (W/O) microemulsions are particularly attractive reactive media for the preparation of particles in nanosize dimensions. These microemulsions consist of nanometer sized water droplets which are dispersed in a continuous oil medium and stabilized by the surfactant accumulated at the oil/water interface. Such microemulsions exhibit low polydispersity, i.e. size uniformity water droplets. If ionic reactants are confined to the aqueous interior, particles can be precipitated primarily to the dimension of water droplets. Thus, we can control the particle size by adjusting the size of the aqueous core of the microemulsion. A NCT patent is pending for "The Microemulsion method for Metal Oxide Nanocrystals", Appendix B, patent 2.

Procedure used to synthesize nanoparticles of Y_2O_3:Tb

The synthesis of colloidal Y-Tb mixed hydroxide was achieved by mixing equal volumes of two sets of microemulsions. The microemulsions contain surfactant, oil, co-surfactant, butanol, water phases, Yttrium and Terbium salts and hydroxides. The microemulsions were mixed at room temperature under thorough stirring. The precipitate of mixed Y-Tb hydroxide was centrifuged at various rpm speeds. The precipitate was washed with water to remove the surfactant and oil from the particle surface. For the transformation of mixed hydroxide to oxide, samples were heated at different temperatures in the 150 to 700 °C range, in various atmospheres.

To completely remove the surfactant, the precipitate was thoroughly washed with water, subsequently sonicated, and finally collected by ultracentrifuging. The number of water washes, the speed and duration of the sonication, and the speed and duration of the centrifuge process play a critical role in "cleaning" the nanoparticle surface from residual contaminants.

Variations of the above procedures were also used to synthesize Gd_2O_3:Tb nanocrystalline X-ray phosphors. The X-ray response of Gd_2O_3:Tb nanophosphors was especially encouraging so no attempt was made to synthesize PbO:Tb so far. In-house Scanning-Electron-Microscopy, and Transmission-Electron-Microscopy and Atomic-Force-Microscopy data obtained at Oakridge National Laboratory confirmed that the nanocrystal size is in 2-5 nanometer range.

Task 2: Characterization and optimization of nanocrystalline phosphors

- Set up a pulsed Molybdenum target X-ray system for testing phosphors at 17.5 keV
- Measure the quantum efficiency of these phosphors under UV and X-ray excitation
- Optimize the quantum efficiency as a function of particle size.
- Set up a detection system for measuring decay times in the range of 100-nsec and 10-msec
- Measure and optimize the time decay under pulsed X-ray excitation

A used TREX-LORAD M-II X-ray mammography system was set-up in the laboratory in order to characterize and optimize the performance of our phosphors. The exciting X-ray energies can be varied in the 25-50 KVp range. The X-ray pulse duration is in the 0.2-5 second range. To measure the phosphor light output under X-ray excitation, a *Si* photodetector is placed underneath the plate containing the phosphor powder. A conventional KODAK LANEX mammography screen and standard $Gd_2O_3S{:}Tb$ X-ray phosphor are used to normalize our results.

For the UV luminescence evaluation of the nanocrystalline phosphors a SPEX Fluorolog spectroscopy system is used. Again, the nanocrystalline phosphors are measured against the best conventional UV phosphors.
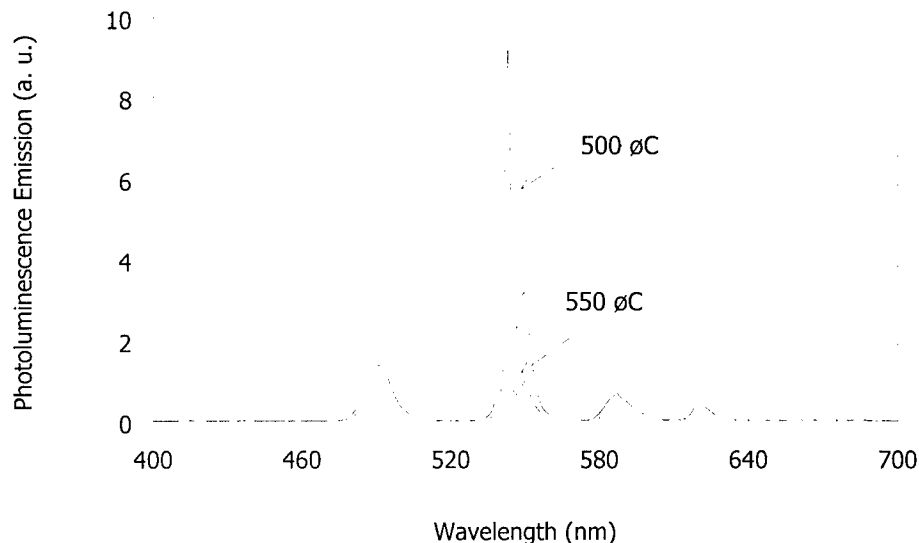
Figure 5. Up to 500°C, the particles retain nanosize dimensions (solid line). Above 550°C, the particles coalesce and have a bulk-like behavior (dotted line).

By heat-treatment in different atmospheres, sonication, *Tb*-dopant concentration and nanocrystal-size optimizations, we were able to reach 80% of the best commercial

phosphor luminescence (Y_2O_2S:Tb) at 248 nanometer excitation. The dramatic effect of nanocrystalline-phosphor annealing on the luminescence efficiency is shown in Fig. 5. By increasing the temperature from 500 to 550 °C, the luminescence efficiency drops by 60% due to the temperature-related increase in particle-size.

Time-decay measurements of Y_2O_3:Tb and Gd_2O_3:Tb nanocrystals were performed at the Naval Research Laboratories. The time-decay was measured to be a few microseconds, which is almost an order of magnitude faster than the millisecond response of standard phosphors. We interpret the phosphor time-decay increase as a result of the quantum-confinement.

The luminescence efficiency of our optimized nanocrystalline phosphors, under 248 nanometer UV excitation, is 80% of the standard phosphors. Under X-ray excitation, however, the optimized nanocrystalline phosphors exhibit a luminescence efficiency that is 25% of the standard Y_2O_2S:Tb and Gd_2O_3S:Tb phosphors. Annealing, sonication, and synthesis modifications did not produce nanocrystalline phosphor with X-ray luminescence efficiency close to that of standard X-ray phosphors. For this reason we decided to proceed with the microchannel-plate screen concept in which we obtained extremely encouraging results.

Microchannel-Plate Screen

Microchannel plates of 5-cm x 5-cm size with a channel-diameter size of 10 μm have been purchased from a commercial vendor[1]. A channel size of 10 μm will enable NIC to achieve a resolution of 40 lp/mm in the analog mode. Proprietary electrophoretic and gravitational techniques have been used to fill the 10-micron sized channels with phosphors. To achieve dense packing inside 10-micron channels, standard X-ray phosphors of 2-5 microns were evaluated and used, Fig. 6.
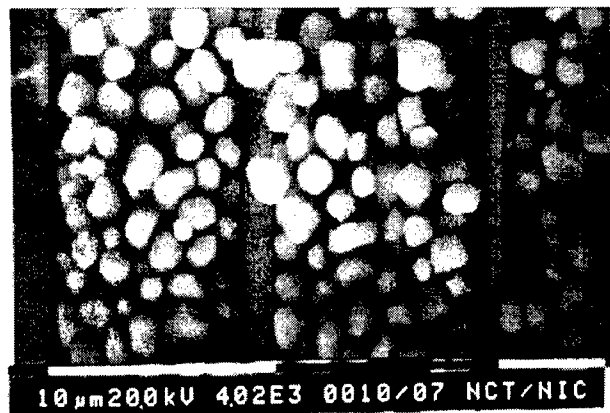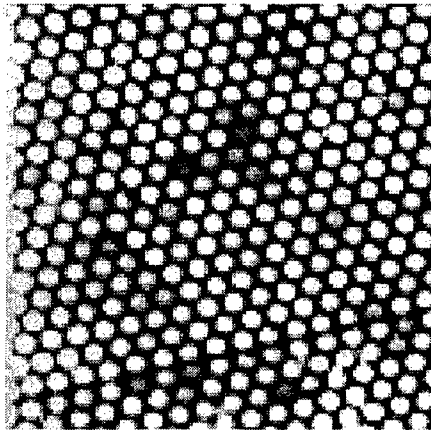

Figure 6. Photograph of packed microchannels as recorded by a Scanning Electron Microscope (SEM).

Proprietary processes for channel-wall reflective coatings have been developed. The guiding of X-ray generated-light, emitted by the phosphor packed inside the channels, has

---

[1] These plates are made for different applications and are available from several vendors.

been demonstrated. The microchannel-wall reflective coatings prevent "cross-talk" between light generated in adjacent channels (see light guiding in Fig. 3).

The scanning-electron-microscope (SEM) photograph of Figure 6 shows a cross sectional view of a 10-μm channel packed with phosphor. This plate, when excited under ultra-violet light shows light emission and light guiding in the phosphor filled 10-μm channels, Figure 7. In this optical-microscope photograph, the uniform distribution of light in channels can be clearly observed. This translates to reduced spatial-noise, which is critical for improving the resolution and the contrast of digital images. Figure 3 depicts a simulated X-ray confinement and transmission pattern through the microchannel-plate. As shown in figure 3, the distance between the centers of two adjacent 10-μm diameter channels is 12μm. This would correspond to a resolution of 40-lp/mm in the analog mode and 24-lp/mm in the digital mode. The resolution of 24-lp/mm in digital mode is a consequence of the hexagonal arrangement of the circular microchannels. When plates with 10-μm square microchannels are used, a resolution of 40-lp/mm in both digital and analog modes is expected. A NCT patent on the microchannel-plate screens is pending, Appendix B, patent 3.

Figure 7. An actual microscope photograph of a NCT phosphor-filled microchannel-plate under 254-nm UV excitation. The channel diameter size is 10-μm and the center-to-center spacing is 12-μm.

Preliminary X-ray-to-light contrast/resolution measurements are currently underway and are being used to optimize the process and design parameters, such as the amount of phosphor, thickness and depth of channels, and reflective light-guiding coatings.

Preliminary Resolution Measurements

Microchannel plates of 10-μm diameter size were filled with standard X-ray phosphors and sealed using a proprietary process developed at NCT. Data on the resolution of NCT plates were collected under the supervision of Prof. Frank Carroll M.D., of Vanderbilt University, one of the nation's leading radiologists. Tests using the NCT-plates and a 20-lp/mm test-pattern-mask (commonly referred to as a phantom), yielded very sharp images. Currently, line-pair-resolution phantoms are capable of resolving up to 20-lp/mm. Mathematical analysis of the images (Modulation-Transfer-Function) confirms the theoretically expected resolution of 40-lp/mm. This resolution is two times higher than that of the best Kodak analog screen/film system currently used in mammography.

9

Key Research accomplishments

- Nanocrystalline phosphors of green-emitting Y_2O_3:Tb and Gd_2O_3:Tb were synthesized using patented wet-chemistry processes. The nanocrystalline-particle sizes were in the 2 - 5-nm range.

- The luminescence efficiency of the nanocrystalline phosphors, under 248-nm UV excitation, is 80% of the standard phosphors. Under X-ray excitation, the nanocrystalline phosphors exhibit a luminescence efficiency that is 25% of the standard Y_2O_2S:Tb and Gd_2O_3S:Tb phosphors.

- The time-decay of nanocrystalline phosphors is a few microseconds compared to milliseconds for standard phosphors.

- Microchannels of 6-15 μm diameter were packed with standard X-ray phosphors. *Scanning-Electron-Microscopy* showed very dense packing of phopshors inside the channels.

- Resolution measurements were performed on 10-μm microchannel-plates (packed with standard X-ray phosphors), using 20-lp/mm test-pattern-masks. Mathematical analysis of the images yielded a resolution of 40-lp/mm

Reportable outcomes

- Journal Paper

R. N. Bhargava, V. Chhabra, B. Kulkarni and J. V. D. Veliadis, "Transformation of Deep Impurities to Shallow Impurities by Quantum Confinement", Phys. Stat. Sol. (b) **210**, 621 (1998).

- Patents

1. "Composite nanophosphor screen for detecting radiation", R. N. Bhargava. Patent Approved.

2. "Microemulsion method for Metal Oxide Nanocrystals", V. Chhabra, B. Kulkarni, R. N. Bhargava. Patent Pending.

3. "Composite nanophosphor screen for detecting radiation having optically reflective coatings", R. N. Bhargava, N. Taskar, V. Chhabra, J. V. D. Veliadis. Patent Approved.

Conclusions and Future Work

The goal of this research is to fabricate X-ray mammography screens with dramatically increased contrast/resolution capabilities. A conventional X-ray phosphor screen has a thickness of about 50 to 200 microns (μm) and consists of phosphor particles with a mean size between 3 to 10 μm. The light generated in the phosphor screen by the incident X-rays scatters over the thickness of the screen material. As the light scatters, it spreads out which results in loss of spatial resolution and contrast.

To overcome the severe light scattering that stems from the phosphor screen thickness, without compromise in X-ray absorption, two approaches have been rigorously investigated. The first approach is to manufacture screens based on a novel type of efficient phosphors: nanocrystalline phosphors. The second approach is to fill microchannel plates with nanocrystalline or micron-sized phosphors. The X-ray-induced light is now transmitted and confined within the microchannel, which operates like an optical-fiber waveguide.

Under X-ray excitation, the nanocrystalline phosphors exhibited luminescence efficiency that is 25% of the standard phosphors. A significant increase in nanocrystalline X-ray efficiency is needed before these particles are incorporated in mammography screens.

Microchannel plates of 10-μm diameter size were filled with standard X-ray phosphors and sealed using a proprietary process developed at NCT. Resolution measurements using the NCT-plates and a 20-lp/mm phantom, yielded very sharp images. Currently, line-pair-resolution phantoms are capable of resolving up to 20-lp/mm. Mathematical analysis (Modulation-Transfer-Function) showed that the images have a resolution of 40-lp/mm. This resolution is two times higher than that of the best Kodak analog screen/film system currently used in mammography.

Based on the experimentally documented success of the microchannel-plate screen, the future research will focus on optimizing these screens for commercial analog and digital mammography systems. By lifting the scattering-related resolution/contrast limitations of present X-ray screens we will greatly improve the capabilities of the mammogram as a detection tool.

11

REFERENCES

[1] X. Zhou and R. Gordon, "Detection of early breast cancer: an overview and future prospects", Crit. Rev. Biomed. Eng., vol. 17, 203-55 (1989).

[2] S. F. Hurley and J. M. Kaldor, "The benefits and risks of mammographic screening for breast cancer", Epidemiol. Rev., vol. 14, 101 -30 (1992).

[3] T. G. Lange and E. S. de Pardes, "Pitfalls in mammography", Applied Radiology, 13-24, Sept. 1990.

[4] R. E. Bird T. W. Wallace and B. C. Yankaskas, "Analysis of cancer missed at screening mammography", Radiology, vol. 184, 613-7 (1992).

[5] J. Weinreb and G. Newstead, "Controversies in breast MRI", Magnetic Reson. Q., vol. 10, 67-83 (1994).

[6] E. M. Paterok, H Rosenthal, S. Richter, and M Sabel, "Occult calcified breast lesions", Eur. Radiology, vol. 3, 138-44 (1993).

[7] K. Kerlikowske, D. Grady, J. Barclay, E. A. Sickles, A. Eaton, and V.Ernester, "Positive predictive value of screening mammography by age and family of breast", J Am. Med. Assoc., vol. 270, 2444-50 (1993).

APPENDIX A

Journal Paper
R. N. Bhargava, V. Chhabra, B. Kulkarni and J. V. D. Veliadis, "Transformation of Deep Impurities to Shallow Impurities by Quantum Confinement", Phys. Stat. Sol. (b) **210**, 621 (1998).

Transformation of Deep Impurities
to Shallow Impurities by Quantum Confinement

R.N. Bhargava, V. Chhabra, B. Kulkarni, and J.V. Veliadis

Nanocrystals Technology, P.O.Box. 820, Briarcliff Manor, NY 10510, USA

We report for the first time how the optical transitions associated with localized levels of a rare-earth impurity can be modulated by quantum confinement. The effect of quantum confinement on impurity critically depends on the size of the host crystal. The variation of absorption and luminescence efficiency of Tb^{3+}-ion doped Y_2O_3 is discussed within the framework of the quantum confined atoms.

Introduction.   The localized states are useful centers in semiconductors and insulators, since they yield a well-defined 'characteristic' optical signature. Usually such emission characteristics are independent of the host in which these dopants have been incorporated. For example, the localized centers such as rare earth and transition metal impurities are the best line emitting phosphors for display and lighting industry. The biggest drawback of these localized states is that the transfer of carriers from the host to the center is rather slow. This slow capture process thus limits the luminescence efficiency provided by these localized states.

These localized states are similar to deep states in many respects. For example they possess the following characteristics.

1. The energy levels associated with the localized levels are typically much deeper than the normal effective mass energy.

2. The thermalization rates from these states are small.

3. The localized states similar to deep states can dominate the recombination kinetics, yet they do not play a significant role in modulating the conductivity of the semiconductor.

4. In semiconductors or insulators the localized states act more like deep states but frequently are neutral centers. The charge neutrality has been exploited to yield excellent phosphors.

In this paper, we report for the first time how the optical transitions associated with localized levels of a rare-earth impurity can be modulated by quantum confinement. The effect of the quantum confinement on impurity critically depends on the size of the host crystal. As the size of the host decreases, the degree of the confinement and its effect increase. This type of quantum confinement allows us to change the properties of a localized impurity. In future using similar size control, we hope to modulate the known deep states in semiconductors. Before we discuss the recent results, we want to describe the evolutionary background work of modulating the luminescence properties of the localized or deep states and which eventually led to the model of quantum confined atoms.

25*

The properties of atoms are well defined and known extensively. The incorporation of an atomic ion (activator or dopant) in semiconductors and phosphors have provided the desirable and controllable optoelectronic properties. The control of conductivity and light emission in a given host material is achieved by the incorporation of activator-ions whose concentration typically varies in the range of 10^{-6} to 10^{-2}. Indeed, this small concentration of the activator ions, which provides the precise control of the extrinsic optical and electrical properties of the host material and devices, is the basis of semiconductor industry. How can we improve the capture or emission role of an impurity (dopant/activator) in a given host (semiconductor/insulator) is the subject of this paper. We believe that the enhancement of the 'activity associated with the impurity' would create next generation devices with higher efficiency and faster speed to impact all phases of the industry.

The choice of the atomic impurity in a host determines the eventual property of the host. For example, the impurities, which are quite localized, would yield an optical emission without their internal transition strongly perturbed by the host lattice. In case of electrical conductivity the choice is to have an atomic impurity which replaces the host lattice without disturbing the local electronic/lattice structure, and only provides an additional charge carrier for the extrinsic conductivity. To enhance the 'activity associated with the impurity' our effort in the past five years has been to incorporate a localized impurity in a nanocrystalline size host and study the luminescence properties of the activator when the host is excited, in particular the variation of the luminescence efficiency of the extrinsic activator-ion as a function of the size of the host nanocrystal. As the size of the nanocrystals decreases there is an enhancement of the luminescence efficiency.

Model of $ZnS:Mn^{2+}$.   The first results reported on doped nanocrystalline (DNC) materials were on $ZnS:Mn^{2+}$ [1 to 3]. In this DNC system, it was observed for the first time that the efficiency of the Mn^{2+} emission in nanocrystalline powder was higher than in the bulk phosphor. Furthermore, the luminescence decay time of the Mn^{2+} emission was about 10^5 times shorter than what was in the bulk ZnS. Both of these effects were observed when the size of the nanocrystals was smaller than the Bohr radius of the semiconductor. These two effects were explained on the basis of hybridization of the electrons and holes with localized d-states of the Mn^{2+}. It was anticipated that such a change in the oscillator strength of the Mn^{2+} d-states occurred because of the large overlap of the s-electrons of the host conduction band and the d-electrons of the localized impurity. The enhancement of this overlap should result in faster transfer to the impurity and thereby increase the efficiency. Additionally, the relaxation of the selection rules of the internal transition of Mn^{2+} from forbidden to allowed resulted in a large change in the luminescence decay time.

To test the concept beyond the earlier hypothesis of hybridization proposed for $ZnS:Mn^{2+}$ doped nanocrystals, and further investigate the reasons for the change in the oscillator strength of the internal states of the activator, we have chosen a new system of doped nanocrystalline system. In this new host and impurity combination the particle size is always larger than the Bohr diameter. The chosen system is $Y_2O_3:Tb^{3+}$, a well-known phosphor. In this case the electrons and holes of the host would not be considered either weakly or strongly confined since the Bohr diameter of electrons in Y_2O_3 is about 1 nm while the particle sizes are in the range of 5 nm. This is in contrast

to the ZnS:Mn case where the Bohr diameter was 5 nm and was comparable to the diameter of the ZnS nanoparticle. In nanosize particles in the range of 2 to 5 nm, we observe a significant increase in the luminescence efficiency. To explain these results, a new model of doped nanocrystals is proposed where the change in the oscillator strength is a result of the quantum confinement of a localized atom by the boundary of the host. We call the system "Quantum Confined Atom". The "Quantum Confined Atom" henceforth referred as QCA, characterizes a new class of materials where the properties of a localized impurity are modulated in a quantum dot. This modulation as discussed in this paper for the first time, is attributed to the interaction between the excited states of the localized impurity and induced carrier in the nanocrystal (quantum dot). Before we can discuss the model of QCA and the results of our investigation, we want to describe the details of the rare-earth induced luminescence in bulk oxides, which are insulators with energy band gaps in excess of 6 eV.

The characteristic luminescence of rare-earth ion [4] is attributed to the 4f shell, which is not entirely filled. The electrons of this shell are screened by the outer electron shells and as a result yield a number of discrete energy levels. Since the presence of the crystal lattice hardly effects the position of these levels, these transitions remain invariant for an isolated ion or for an incorporated ion in various hosts. The filled 4f shells contain 14 electrons. The state with a completely filled (Lu^{3+}) and half-filled (Gd^{3+}) electron shell configuration is the most stable. In case of Tb^{3+} there are 8 electrons (represented as $4f^8$ which is half-filled $4f^7$ plus one). The 4f shell readily releases an electron and the intra-ionic transition $4f^8$–$4f^7 5d$ takes place at relatively low energy. Since the 5d orbit lies at the surface of the ion, it can strongly be influenced by the lattice. The excited 5d state is strongly influenced by the electric field of the surrounding ions (i.e. crystal field) and results in the splitting into a number of levels. The number of these levels is determined by the crystallographic symmetry at the position of the rare-earth ion. Since the crystal-field splitting varies considerably from one lattice to another, so too does the spectral position of the absorption bands of a particular 4f–5d transition. The 4f–5d transition is allowed for both absorption and emission process and hence we observe intense absorption bands in the UV region for all oxide hosts. Usually we observe a number of 4f–5d bands due to crystal field splitting of the excited d-level.

Thus, in the case of Tb^{3+} in Y_2O_3, the excitation in the 4f–5d absorption bands is followed by green $^5D_4$–$^7F_5$ emission. The excited electrons from $4f^7$–5d state decay stepwise to the $^5D_3$ or $^5D_4$ state, thereby giving lattice phonons. The $^5D_4$ to ground state transition leads to green $^5D_4$–$^7F_5$ and blue $^5D_4$–$^7F_6$ emission. Although the position of the $4f^7$–5d absorption and excitation bands depends on the nature of the lattice, the green ($^5D_4$–$^7F_5$) emission does not. The internal transition among the $4f^8$ is parity and spin forbidden. However, the influence of the crystal lattice and slight admixing of the ^5D and ^7F state leads to partially allowed transition. This results in a luminescence lifetime in the range of a few milliseconds. The green emission depending upon the excitation wavelength is very efficient. In case of Y_2SiO_5:Tb^{3+}, the photoluminescence quantum efficiency is close to unity when excited by the 254 nm line of a Hg lamp.

We have recently demonstrated that when we have 2 to 5 nm size Y_2O_3:Tb^{3+} nanoparticles, the efficiency of Tb^{3+} green emission in Y_2O_3 is as good as in Y_2SiO_5:Tb^{3+} in spite of the fact that the excitation spectra in the two systems are quite different. This is due to a new way of modulating the interaction of Tb^{3+} ion with the host Y_2O_3

nanocrystals. How the modulation of the core states is achieved is the subject of this paper.

The confinement of the atomic impurity achieved in a nanocrystalline size host allows transferring the energy efficiently to the atom. The caged atom derives the oscillator strength from the host in a very different manner than known heretofore. The QCA model is developed on the basis of the changes observed in the optical properties of a localized impurity as a function of the size of the nanocrystalline host. The choice of the atom and the host was where recombination properties of the phosphor were known. In this paper we describe the luminescence properties of $Y_2O_3:Tb^{3+}$, a well-known phosphor. Both the variations of the absorption and the subsequent emission are discussed in detail.

Experimental Results. All the samples were prepared using microemulsion technique. Because of the proprietary nature of the process, we at this time cannot describe the processing steps but the experiments done to identify and characterize the key properties are described below.

As-grown samples are doped with about 5% of Tb and are primarily hydroxide. The conversion of hydroxide to oxide is normally achieved in several annealing steps. The size and its distribution of as-grown samples were analyzed using Atomic Force Microscope (AFM). AFM images showed that most of the nanocrystals were in the range 1 to 3 nm. Transmission Electron Microscopy (TEM) was also performed to assess the size of the nanoparticles directly. In our case, the Tb-ion emission characteristics do not change with size as long as the size of nanocrystals remains below ≈ 10 nm. When the particle sizes are >10 nm the emission characteristics are more bulk-like.

Extensive measurements were performed to study the variation of efficiency and spectral features as the size of the particles varied from nanosize to bulk-like. The changes in the efficiency are strongly functions of the particle size and particle-size distribution. The size distribution is a critical function of the annealing temperature. A higher temperature leads to larger particles eventually yielding bulk-like optical spectral features. This probably occurs when the size of the particles is in range of 10 nm or larger.

We have performed Photoluminescence Excitation (PLE) and Photoluminescence (PL) and Selective Photoluminescence (SPL) measurements. In PLE the absorption spectra associated with the generation of green emission $^5D_4-^7F_5$ are obtained, as shown in Fig. 1. The spectral features in PLE show a transfer mechanism of the excited carriers from $4f^7-5d$ bands (where the absorption occurs) to $4f^8$-manifold of the Tb^{3+} ion. For example, for the sample shown in Fig. 1, the peak absorption for the most efficient transfer to $^5D_4-^7F_5$ (543 nm) occurs at 246 nm. This is quite different from what is observed in case of bulk $Y_2O_3:Tb^{3+}$ phosphor samples.

To understand the variation of the efficiency, we compared the light output of the nanocrystals and the standard phosphors under 254 nm excitation in two different modalities. In the first case, the light output of nanocrystalline phosphor was compared with standard Tb-based phosphor ($Gd_2O_2S:Tb^{3+}$ and $Y_2SiO_5:Tb^{3+}$) using UV-lamp and a calibrated photometer. In the second case, the peak-emission spectral intensity of nanocrystalline phosphor and a standard phosphor were compared under identical excitation conditions in a spectrometer. Both techniques gave consistent results.

One of the interesting comparisons is that the PL efficiency of the bulk $Y_2O_3:Tb^{3+}$ samples is significantly lower than that of the nanocrystalline (NC) $Y_2O_3:Tb^{3+}$ samples.
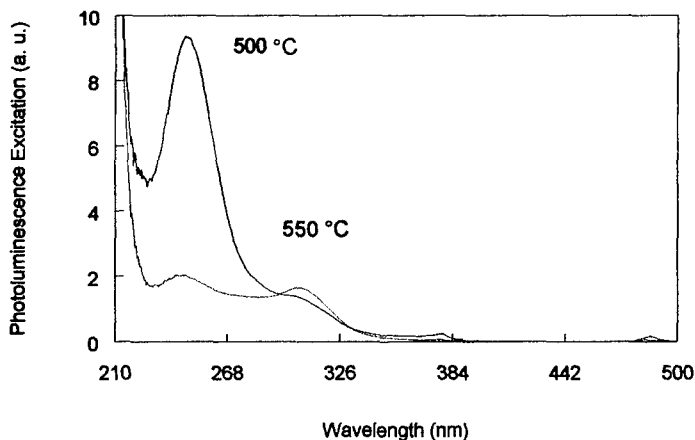
Fig, 1. PLE of a nanocrystalline (upper curve) and a bulk-like sample (lower curve). The green emission at 543 nm was used as the detection wavelength

In fact, the nanocrystalline samples heated to temperatures over 500 °C result in spectral features similar to bulk $Y_2O_3 : Tb^{3+}$ samples. This is shown as 550 °C sample in Fig. 1. The bulk-like samples show a four to five times lower PL efficiency than nanocrystalline $Y_2O_3 : Tb^{3+}$ samples. The physics of this will be discussed later. This clearly establishes that smaller NC particles are more efficient than larger NC particles or bulk-like samples.

The PL emission characteristics in the visible region were obtained with 254 nm excitation. This particular excitation wavelength was used because most of the phosphors are characterized at this exciting wavelength. All fluorescent tubes use this Hg line for the generation of light. Fig. 2, shows the PL spectra of a NC and a bulk-like $Y_2O_3 : Tb^{3+}$ sample. The crystal-field splitting which is observed clearly in bulk samples is also ob-
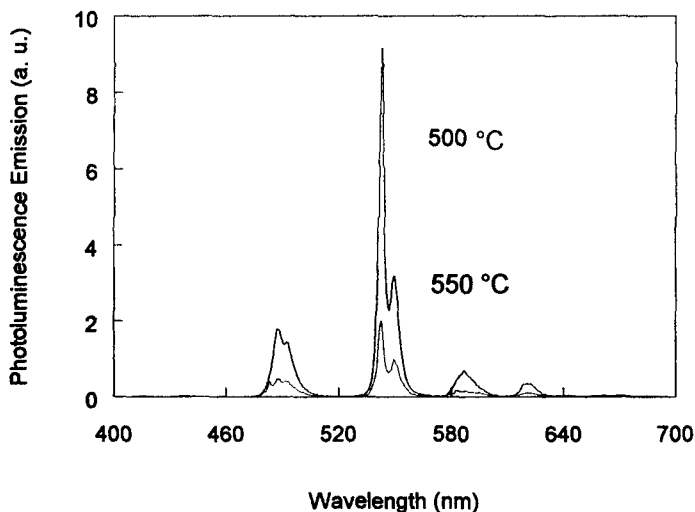

Fig. 2. PL of a nanocrystalline (upper curve) and a bulk-like sample (lower curve) for 254 nm excitation
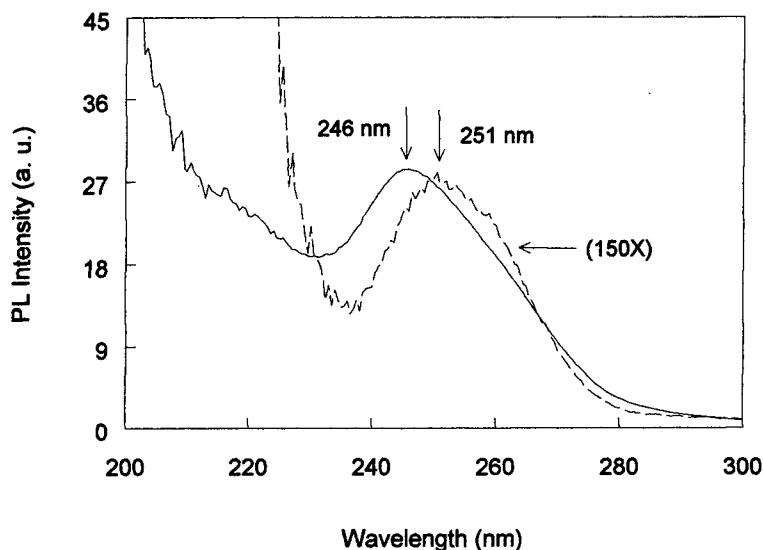
Fig. 3. PLE of nanoparticles with the detector set at 543 nm ($^5D_4-^7F_5$) and 417 nm ($^5D_3-^7F_5$). The shift is due to the presence of different sized particles

served in bulk-like samples which were heated at 550 °C. However, the intensity of both bulk and bulk-like samples is significantly lower than that of NC-Y_2O_3:Tb^{3+}. The photoluminescence (PL) efficiency of Y_2O_3:Tb^{3+} nanocrystalline (NC) samples, at 254 nm excitation, is comparable to the best-known green phosphors such as Y_2SiO_5:Tb^{3+} and Gd_2O_2S:Tb^{3+}.

We have used PLE, PL and SPL not only to study the variation of the spectral features but also to isolate the contribution of different particle sizes. In Fig. 3, we have plotted the PLE spectra with detector wavelengths set at $^5D_3-^7F_5$ (417 nm) and $^5D_4-^7F_5$ (543 nm) for the same sample. It is clear that the nanoparticles responsible for the 417 nm emission show a PLE peak at 251 nm, while the nanoparticles responsible for the 543 nm emission shows a PLE peak at 246 nm. This shift of 5 nm ($\approx$100 meV) suggests that we have a size distribution and different size particles have different PLE spectra. This was also confirmed by observing the changes in the PL spectra as the excitation wavelength was varied from 220 to 330 nm. The variation of exciting radiation, normally referred as SPL, allows us to study the variation of the PL spectral features for different exciting radiation. This is very similar to SPL studies performed to isolate the contribution of different impurities in the luminescence studies of semiconductors [5]. In our study, the contribution of different size particles was established by measuring the ratio of 417 and 543 nm emission for different excitation wavelengths. The reasons for this variation will be explained in the following section.

Quantum Confined Model. To explain the results of size variation of the quantum efficiency we have drawn the standard configuration coordinate (CC) model for Tb^{3+} in Y_2O_3 [6]. In Fig. 4, we have schematically included the effect of the distortion imposed by the quantum confinement on $4f^7$–5d bands. This is shown as three different CC parabola, marked A, B and C. These represent the bulk, medium-size nanocrystals

(>5 nm) and small-size nanocrystals (<5 nm), respectively. We associate the small nano-
particles with the highest energy PLE peak. Before we explain the variation of the
quantum efficiency of $Y_2O_3:Tb^{3+}$ nanocrystalline particles on the basis of CC model
we summarize the key observations:

1. The peak of the PLE (absorption) moves to lower energy as the size of the nano-
particles increases. In Fig. 4, this is shown as absorption levels A, B and C. Typical
values of these transitions are 4.0, 5.0 and 5.6 eV, respectively.

2. The intensity of the absorption peak (PLE) decreases as the peak position moves
to the lower energy. This suggests that the product of the absorption and emission
intensity (i.e. PLE) is largest for the smallest particles.

3. In Fig. 4, as the particle size decreases the transfer mechanism of excited carriers
shifts. In case of A, the carriers go through directly downwards in a Tb-ion energy
manifold, resulting in a slow process. Since the $^5D_3-^7F_5$ are forbidden, we observe a
weak 417 nm emission line. However, as the particle size changes to medium size nano-
crystals, the intensity of the 417 nm transition improves since the transfer to $^5D_3$ level
occurs directly without going through intermediate levels, as depicted in the configura-
tion coordinate diagram B. This is due to the confinement of Tb ions imposed by the
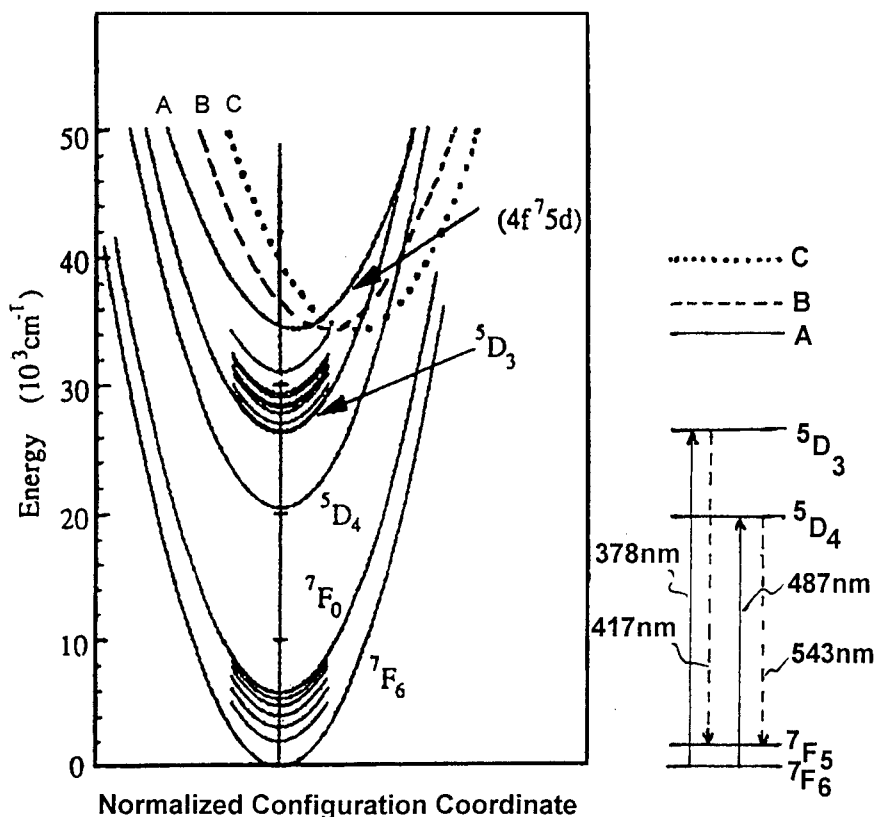host boundary. When the particle size is further reduced, as in case of C, the transfer

Fig. 4. Configuration coordinate model of Tb in Y_2O_3. The A, B, C, levels on the right, represent
the absorption energy peaks for the bulk, medium-size and small-size nanoparticles, respectively

can occur directly to the $^5D_4$ level. This quenches $^5D_3$–$^7F_5$ (417 nm) transition and the efficiency for the green light improves.

4. The CC model in Fig. 4 explains the various changes observed in various samples. These changes are consistent with the fact that upon heating the particle size increases and the efficiency decreases, as shown in Figs. 1 and 2. This was earlier observed in the case of Mn^{2+} in ZnS.

5. The changes in the oscillator strength brought about by the quantum confinement are only present when the carriers are present in the host. The charge transfer modulates the intra-ionic states such as $4f^7$–5d, as a result of quantum confinement there are no changes in the core $4f^8$ states.
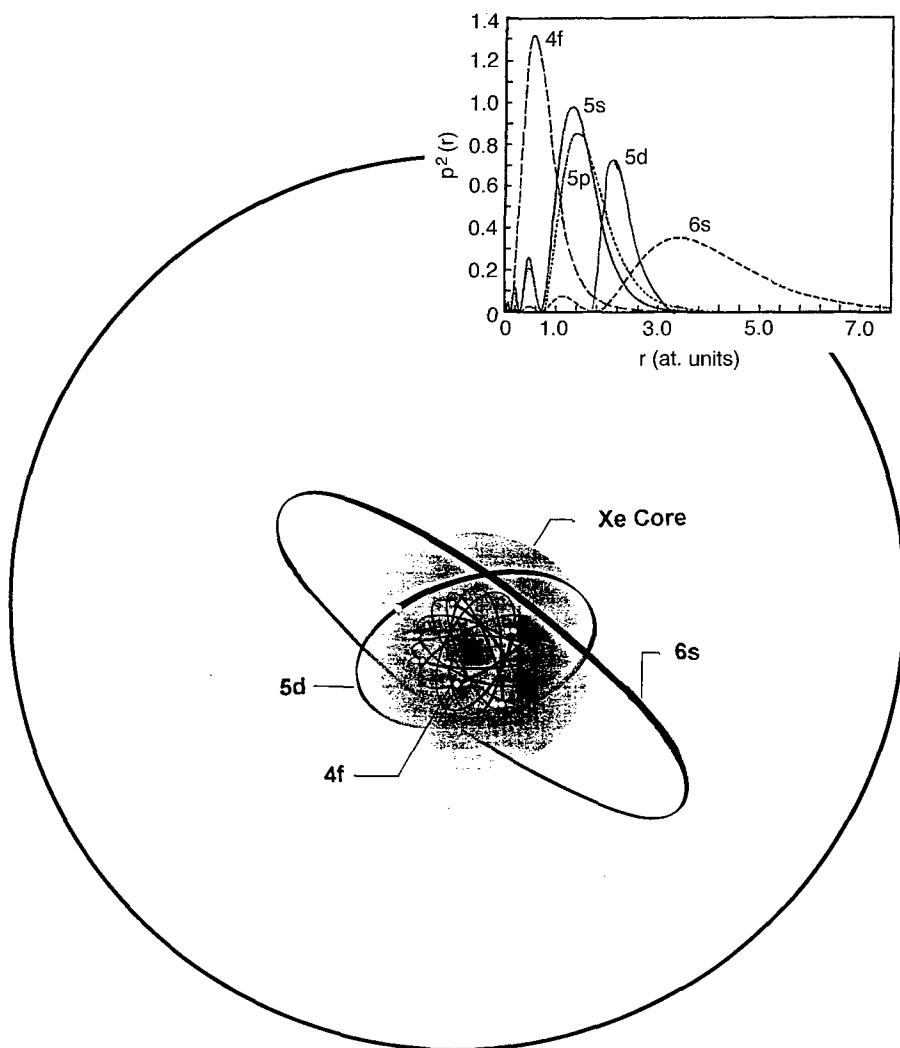

Fig. 5. Quantum confined model of Y_2O_3:Tb nanoparticles. The abscissa scale in the inset is in atomic units (1 a.u. = 0.53 Å)

Considering the significant changes that are observed in doped nanoparticles of size of about 2 nm, we propose the model of QCA. In this model, the excited states of the atom (activator or dopant) do provide a significant overlap with the host boundary. The overlap of the wavefunctions of the host and the extended excited states leads to strong modulation of the excited states of the atom. This modulation subsequently leads to efficient and fast transfer of carriers from the host to the atom. The atom in the 'quantum mechanical cage' is given in Fig. 5. Not only the 5d states of Tb ion but also other higher excited states such as 6s, 6p etc. begin to play a role in the transfer mechanism. An efficient transfer of carriers is expected to impact all the opto-electronic devices.

The confinement of localized states in semiconductors and insulators has resulted in enhancing the charge transfer to the impurity. This process of caging the atom and modulating the nature of the deep or localized states, has transformed some of the properties of these localized states to that of shallow states. The enhanced interaction and rapid charge transfer of these quantum-confined atoms could be used to develop a new class of dopants in future.

In summary, quantum confined atom is a nanocomposite made of isolated few atoms in a quantum dot which results in materials where the properties of atoms are only modulated without changing its signature. In fact, the properties of the atoms are retained, protected and significantly amplified via its interaction with the host. Such a nanocomposite system offers numerous possibilities for the next generation devices in the nanosize range.

References

[1] R. N. Bhargava, D. Gallagher, X. Hong, and A. Nurmikko, Phys. Rev. Lett. **72**, 416 (1994).
[2] R. N. Bhargava, D. Gallagher, and T. Welker, J. Lum. **60**, 275 (1994).
[3] R. N. Bhargava, J. Lum. **70**, 85 (1996).
[4] G. Blasse and B. C. Grabmaier (Ed.), Luminescent Materials, Chap. 2, Springer-Verlag, Berlin 1994.
[5] P. J. Dean, D. C. Herbert, C. J. Werkhoven, B. J. Fitzpatrick, and R. N. Bhargava, Phys. Rev. B **23**, 4888 (1981).
[6] A. Daud, M. Kitagawa, S. Tanaka, and H. Kobayashi, Tattori University Rep. (Japan) **25**, 153 (1994).

APPENDIX B

<u>Patents</u>

1. "Composite nanophosphor screen for detecting radiation", R. N. Bhargava. Patent Approved.

2. "Microemulsion method for Metal Oxide Nanocrystals", V. Chhabra, B. Kulkarni, R. N. Bhargava. Patent Pending.

3. "Composite nanophosphor screen for detecting radiation having optically reflective coatings", R. N. Bhargava, N. Taskar, V. Chhabra, J. V. D. Veliadis. Patent Approved.

Final Report
This has been a one year research effort.

Presentations
1. R. N. Bhargava, V. Chhabra, B. Kulkarni and J. V. Veliadis, "Transformation of deep impurities to shallow impurities by quantum confinement", *The 8ᵗʰ International conference on shallow-level centers in semiconductors*, Montpelier, France, July 28-31, 1998.
2. R. N. Bhargava, V. Chhabra, B. Kulkarni and J. V. D. Veliadis, "Transformation of Deep Impurities to Shallow Impurities by Quantum Confinement", Phys. Stat. Sol. (b) **210**, 621 (1998).

Salaried Personnel
R. N. Bhargava
J. V. D. Veliadis
V. Chhabra

MCMR-RMI-S   (70-1y)   23 Aug 01

MEMORANDUM FOR Administrator, Defense Technical Information
Center (DTIC-OCA), 8725 John J. Kingman Road, Fort Belvoir,
VA   22060-6218

SUBJECT: Request Change in Distribution Statement

1.   The U.S. Army Medical Research and Materiel Command has
reexamined the need for the limitation assigned to the technical
reports listed at enclosure. Request the limited distribution
statement for these reports be changed to "Approved for public
release; distribution unlimited." These reports should be
released to the National Technical Information Service.

2.   Point of contact for this request is Ms. Judy Pawlus at
DSN 343-7322 or by e-mail at judy.pawlus@det.amedd.army.mil.

FOR THE COMMANDER:

Encl   PHYLIS M. RINEHART
                                  Deputy Chief of Staff for
                                    Information Management

Reports to be Downgraded to Unlimited Distribution

ADB241560	ADB253628	ADB249654	ADB263448
ADB251657	ADB257757	ADB264967	ADB245021
ADB263525	ADB264736	ADB247697	ADB264544
ADB222448	ADB255427	ADB263453	ADB254454
ADB234468	ADB264757	ADB243646	
ADB249596	ADB232924	ADB263428	
ADB263270	ADB232927	ADB240500	
ADB231841	ADB245382	ADB253090	
ADB239007	ADB258158	ADB265236	
ADB263737	ADB264506	ADB264610	
ADB239263	ADB243027	ADB251613	
ADB251995	ADB233334	ADB237451	
ADB233106	ADB242926	ADB249671	
ADB262619	ADB262637	ADB262475	
ADB233111	ADB251649	ADB264579	
ADB240497	ADB264549	ADB244768	
ADB257618	ADB248354	ADB258553	
ADB240496	ADB258768	ADB244278	
ADB233747	ADB247842	ADB257305	
ADB240160	ADB264611	ADB245442	
ADB258646	ADB244931	ADB256780	
ADB264626	ADB263444	ADB264797	